Metadata of the chapter that will be visualized online

Series Title	Topics in Current Chemistry	
Chapter Title	A Nanomembrane-Based Nucleic Acid Sensing Platform for Portable Diagnostics	
Chapter SubTitle		
Copyright Year	2011	
Copyright Holder	Springer-Verlag Berlin Heidelberg	
Corresponding Author	Family Name	Chang
	Particle	
	Given Name	**Hsueh-Chia**
	Suffix	
	Division	Department of Chemical and Biomolecular Engineering
	Organization	University of Notre Dame
	Address	46556, Notre Dame, IN, USA
	Email	hchang@nd.edu
Author	Family Name	Senapati
	Particle	
	Given Name	**Satyajyoti**
	Suffix	
	Division	Department of Chemical and Biomolecular Engineering
	Organization	University of Notre Dame
	Address	46556, Notre Dame, IN, USA
	Email	
Author	Family Name	Basuray
	Particle	
	Given Name	**Sagnik**
	Suffix	
	Division	Department of Chemical and Biomolecular Engineering
	Organization	University of Notre Dame
	Address	46556, Notre Dame, IN, USA
	Email	
Author	Family Name	Slouka
	Particle	
	Given Name	**Zdenek**
	Suffix	
	Division	Department of Chemical and Biomolecular Engineering
	Organization	University of Notre Dame
	Address	46556, Notre Dame, IN, USA
	Email	
Author	Family Name	Cheng
	Particle	
	Given Name	**Li-Jing**

Suffix	
Division	Department of Chemical and Biomolecular Engineering
Organization	University of Notre Dame
Address	46556, Notre Dame, IN, USA
Email	

Abstract	In this perspective article, we introduce a potentially transformative DNA/RNA detection technology that promises to replace DNA microarray and real-time PCR for field applications. It represents a new microfluidic technology that fully exploits the small spatial dimensions of a biochip and some new phenomena unique to the micro- and nanoscales. More specifically, it satisfies all the requisites for portable on-field applications: fast, small, sensitive, selective, robust, label- and reagent-free, economical to produce, and possibly PCR-free. We discuss the mechanisms behind the technology and introduce some preliminary designs, test results, and prototypes.
Keywords (separated by '-')	Depletion - Dielectrophoresis - Ion-selective membranes - Limiting-current

A Nanomembrane-Based Nucleic Acid Sensing Platform for Portable Diagnostics

Satyajyoti Senapati, Sagnik Basuray, Zdenek Slouka, Li-Jing Cheng, and Hsueh-Chia Chang

Abstract In this perspective article, we introduce a potentially transformative DNA/RNA detection technology that promises to replace DNA microarray and real-time PCR for field applications. It represents a new microfluidic technology that fully exploits the small spatial dimensions of a biochip and some new phenomena unique to the micro- and nanoscales. More specifically, it satisfies all the requisites for portable on-field applications: fast, small, sensitive, selective, robust, label- and reagent-free, economical to produce, and possibly PCR-free. We discuss the mechanisms behind the technology and introduce some preliminary designs, test results, and prototypes.

Contents

S. Senapati, S. Basuray, Z. Slouka, L.-J. Cheng and H.-C. Chang (✉)
Department of Chemical and Biomolecular Engineering, University of Notre Dame, 46556 Notre Dame, IN, USA
e-mail: hchang@nd.edu

Abbreviations

AC	Alternating current
CNT	Carbon nanotube
DC	Direct current
DEP	Dielectrophoresis
DNA	Deoxyribonucleic acid
FCW	Fluorescence correlation spectroscopy
FET	Field-effect transistor
I–V	Current–Voltage
kb	Kilobase
PCR	Polymerase chain reaction
pM	Picomolar
RNA	Ribonucleic acid
SNP	Single-nucleotide polymorphism
ssDNA	Single-stranded DNA

1 Introduction

A new molecular sensing platform promises to significantly advance existing electrochemical/capacitance/field-effect transistor (FET) sensing technology into a probe-functionalized, multitarget and smart (automated) electrode sensing platform, whose assay time (minutes), detection limit (picomolar concentrations), selectivity (single-base mismatch discrimination), dynamic range, and robustness are orders of magnitude better than the current state-of-the-art techniques. The platform involves no moving parts, no valves, no optical detection, and will be fully automated with regenerable probes for prolonged usage. Most importantly, the assay time is shorter than the hour-long degradation half-life of RNAs, enabling realization of a polymerase chain reaction (PCR)-free nucleic acid detection platform [1]. The new DNA/RNA sensing technology is based on several new on-chip ion-selective membrane and nanoslot technologies developed in our group and elsewhere [2–7].

Development of rapid and portable detection devices for point-of-care application is an important aspect of the modern diagnostics industry for effective detection of diseases in developing countries, from anti-terrorism and biowarfare applications to environmental monitoring, including the detection of harmful organisms on beaches. The most specific sensing platform is the genetic detection platform, which identifies a particular sequence of the target pathogen's genome. As a result of active research in this area, small pretreatment units are now available that can concentrate the pathogens with membranes and beads, lyse cells, and remove chromosomal DNA for amplification in an integrated PCR chip [8].

AU1

However, the key technological bottleneck remains the detection and quantification of the amplified DNAs.

Two gold standards for genetic detection have appeared in the last decade, both involving labeling of fluorophores or quenchers onto the target molecule during PCR amplification: DNA microarray and real-time PCR. DNA microarrays offer sensitivity and large library volume. However, the assay time is long due to diffusion limitations. It also requires periodic rinsing to avoid nonspecific binding. Finally, the fluorescent confocal detection instrumentation is still too bulky and costly for portable applications. Quantification of the number of target DNAs is also impossible. Real-time PCR sacrifices large library volume for rapid and quantifiable detection, higher sensitivity, and good selectivity. However, it still requires expensive and bulky fluorescent detection instrumentation. (Model ViiA^{TM}7 of Applied Biosystems is the size of a small refrigerator and costs US \$200,000.) The main challenge for portable diagnostics is then a miniature label-free nucleic acid sensing platform without any sophisticated instruments and reagents. The elimination of the PCR step would also be advantageous, as it would remove the 30-min thermal cycling time and the need for a PCR unit. In many medical applications, over a million DNA and RNA copies are available in a typical sample volume of 100 μL. Consequently, a detection platform capable of sensing one million copies of DNA/RNA can be PCR-free. For bacterial pathogens, each cell produces a million copies of mRNA and only one copy of DNA. However, the tradeoff for this relative abundance of RNA is its short life-time (less than an hour) due to rapid degradation [1]. Hence, an RNA detection platform with an assay time of less than 1 h (and without reverse-transcription PCR) would be the first RNA detection platform of its kind.

Several label-free field-use DNA/RNA sensing technologies have been intensively studied in the last decade. The most viable field-use sensing technology to date is, in our opinion, electrochemical sensing. Electrochemical sensing with molecular probe functionalized electrode sensors can measure the change in electron-transfer rate upon docking of the target DNA/RNA molecules and redox reporter agents that can magnify this electrochemical current. Because many current carriers and inhibitors in the buffer can affect this electrochemical signal, even in the presence of surface-assembled monolayers (SAM), this sensing technology lacks robustness and is difficult to calibrate [9]. Capacitance, conductance, and FET electrode sensors have also attracted considerable interest recently. For such non-Faradaic sensors, excess charges brought to the surface by the docked DNA/RNA molecules and their associated potential can produce a local change in Debye double-layer conductance/capacitance and subsurface current of the sensor. Conductance measurements are typically insensitive at practical ionic strengths because the presence of the DNA/RNA molecules in the high-conductivity Debye layer would not significantly affect the local conductance [10, 11]. Moreover, the same Debye layer is only a few nanometers thick for practical RNA samples, and only the lower fraction of the charges on the long (>10 kb) linear DNA/RNA is responsible for the capacitance signal, again resulting in low sensitivity [12, 13]. At its current state, conductance/capacitance/FET sensors have a detection limit

113 higher than nanomolar, which translates into 10^8 copies of nucleic acid molecules
114 for practical sample volumes [13], which is too high for field-based detection.
115 Most importantly, the largest drawback of all electrode sensors is their long assay
116 time. At the low target molecule concentrations (picomolar) of practical samples,
117 the diffusion time of long (more than kilobase) nucleic acids to the electrode
118 sensor often exceeds hours, thus rendering such a platform ineffective for rapidly
119 degrading RNA.

120   Several techniques have been suggested for removing the slow transport of long
121 nucleic acid molecules to the electrode sensor. One technique involves the activa-
122 tion of a high voltage at the electrode sensor to electrophoretically attract nearby
123 DNAs [14]. However, this electrophoretic concentration technique is highly non-
124 specific and other like-charge molecules can also be attracted to the sensor.
125 Moreover, for buffers of high ionic strength, the elevated voltage can produce
126 undesirable Faradaic reactions that can produce false current or voltage signals.
127 Internal vortices, generated on microelectrodes by various ingenious but unreliable
128 mechanisms, have also been suggested as a means of concentrating the target
129 molecules towards the sensor [15, 16]. Generation of internal vortices remains,
130 however, an imperfect science. It would be more desirable for the sensor to generate
131 such vortices automatically at a precise location and for the vortices to exhibit a
132 strong electric signal such that they can be detected and automatically controlled;
133 this new technology will be described in Sect. 2.   AU4

134   The missing technologies for portable DNA/RNA diagnostics are therefore a
135 label-free electrode sensor that does not suffer from diffusion limitation (i.e.,
136 short assay time), is highly selective and sensitive, and yet is insensitive to buffer
137 ionic strength and chemical composition. We propose here that the ion-selective
138 membrane sensor technologies, with properly tuned electrokinetic features and
139 dynamic feedback actuation, can meet these specifications. Our group has
140 recently developed an on-chip sol–gel silica fabrication technique [17, 18] and
141 a nanocolloid assembly technique for on-chip membrane synthesis [3]. We have
142 also applied several photocuring polystyrene sulfonate or polyallylamine synthe-
143 sis techniques to fabricate on-chip membranes [19]. Recently, we have developed
144 the technology to fabricate nanoslots on chips [5], which behave like single-pore
145 membranes, for application in diagnostic chips. The membranes are used for
146 molecular detection and involve continuous pumping of the sample solution in
147 a cross-flow (tangential to the membrane surface) format to minimize hydrody-
148 namic resistance. On-chip electrodes control the ionic current and voltage
149 drop across these membrane components to produce the desired phenomena for
150 rapid molecular concentration, transport, and detection. A first-generation
151 integrated chip is shown in Fig. 1 for rapid detection of kilobase DNA with
152 probe-functionalized nanocolloid assemblies (membranes). These passive chips
153 are not automated and do not involve feedback control because they are missing
154 several sensors and activation components that our group has recently developed.
155 We will discuss our recent attempts to add and integrate, via on-chip feedback
156 control circuitry, these new components to the first-generation devices to produce
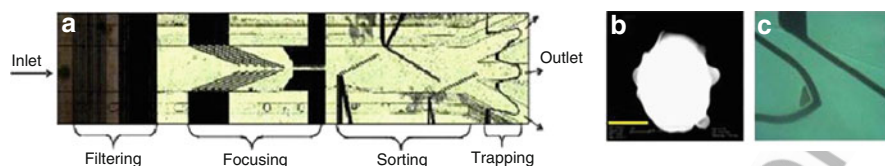157 a multitarget smart DNA/RNA sensor platform.

A Nanomembrane-Based Nucleic Acid Sensing Platform for Portable Diagnostics

Fig. 1 (**a**) Open-flow DEP chip through which nanocolloids functionalized with complementary oligonucleotides are pumped. (**b**) SEM image of a larger colloid (500 nm) with a long oligonucle-otide. *Scale bar*: 200 nm. These nanocolloids are focused, sorted and assembled passively at a microelectrode gate with symmetric and aligned top-down electrode pairs. (**c**) Magnification of a microelectrode gate; the *triangle* shows the trapping of nanocolloids within a micrometer-sized region. DNA solutions, ranging from picomolar to nanomolar concentrations, are then pumped over the nanocolloid assembly (membrane). Fluorescent imaging (see Fig. 6) is used to quantify the specificity and concentration factor, whereas label-free detection yields quantifiable electrical signals (see Figs. 4, 8 and 10)

AU5

2 Membrane-Induced Deionzation, Debye Layer Extension, and Induced Vortex Molecular Concentration

One solution to the robustness issue is to deplete the inhibitors and chemicals around the sensor such that close to deionized water conditions are always produced near the sensor, regardless of the buffer ionic strength and composition. Our laboratory has recently developed several of these depletion technologies based on fabricated ion-selective nanoslots [5–7] and on-chip nanoporous membranes [17, 18]. Significant counterion transport can rapidly deplete the counterions on one side of the membrane. To sustain electroneutrality, the co-ions also deplete rapidly to produce an ion-depleted zone. Sufficiently high DC fields (>100 V/cm) can deionize a 100-µ neighborhood (the depletion zone) near the membrane. The depletion layer with low interfacial ionic strength produces the maximum possible ion current without convection and exhibits a distinct limiting-current plateau in the polarization *I–V* or cyclic voltammetry spectrum (Fig. 2b). This nonlinear *I–V* polarization is not due to electron-transfer reactions but bulk-to-membrane ion flux across the extended and depleted interfacial double layer. Its sensitivity to the interfacial charge in the depleted double layer allows sensitive conduction/capacitance detection of hybridization with the same actuation on-chip electrodes that drive the ion current.

At another critical voltage, the limiting current gives way to a sharp increase in the current, the overlimiting current, which is a very sensitive signature of vortices driven by an extended polarized (Debye) layer at the membrane interface, as shown in Fig. 2b [4, 10, 20]. Nonequilibrium (counter)ion transport across the ion-selective membrane produces an extended polarized layer and nonequilibrium over-potential that is orders of magnitude thicker/higher than the Debye screening length and the equilibrium zeta-potential. As such field-induced polarization is curvature- and perturbation-sensitive, the induced electro-osmotic flow is not uniform and the resulting backpressure can drive microvortices of specific dimension, and linear velocity at
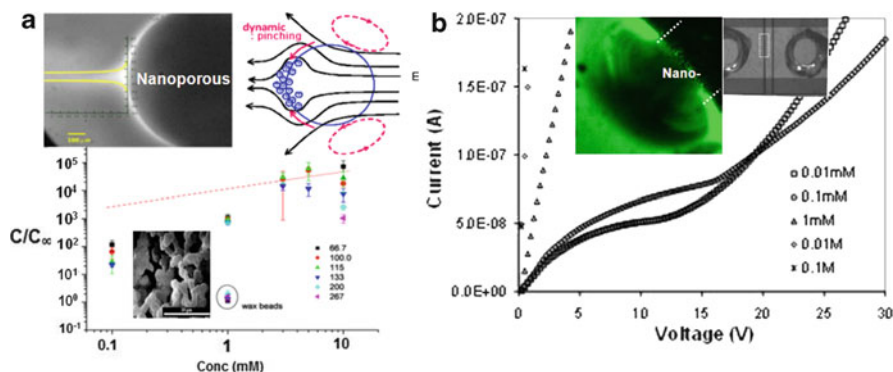
AU8
AU9

Fig. 2 (**a**) Enrichment and depletion across a nanoporous silica granule synthesized within a glass chip by sol–gel chemistry, producing a six orders of magnitude concentration of ions on one side of the granule and a comparable degree of ion depletion on the other side. *Top left*: High magnification SEM image of silica granule with superimposed plot showing ion concentration. *Top right*: Scheme illustrating counterion movement. *Bottom*: Concentration factor c/c_∞ as a function of the ionic concentration (c_∞) of the fluorescent solution for different sizes of silica beads. *Inset*: SEM image of silica beads. (**b**) Depletion of charged fluorescent dye (*left image*) at one entrance of a 50-nm nanoslot between two circular microreservoirs (*right image*). The depletion has a very distinct polarization signature: the current plateaus at a limiting current value when depletion occurs. When vortices are observed in both the silica granule and the nanoslot beyond a critical voltage, the polarization (single-sweep cyclic voltammetry) curve shows a large overlimiting current beyond the limiting current plateau. The same overlimiting current is shown in Fig. 4 before and after hybridization. The plot shows the polarization characteristics of the nanoslot for different ionic concentrations of solution. Linear polarization curves missing the limiting region can be observed for concentrations above 0.1 mM. The disappearance of the limiting region is given by the loss of the ion-selective properties of the nanochannel as a result of decreasing Debye layer thickness inside the nanochannel

186 precise voltage windows. Such microvortices enhance the ion current through the
187 membrane or nanoslot (hence the overlimiting current) and thus exhibit a sensitive
188 polarization or single-sweep cyclic-voltammetry overlimiting signal as shown in the
189 polarization curve in Fig. 2b. This strong conductance signature allows us to develop a
190 smart platform that can generate such vortices on demand. Concentration of the
191 charged dye by five orders of magnitude (shown in Fig. 2a) is mostly due to convective   AU10
192 concentration of the molecules at the stagnation points of the vortices. Other than the
193 distinctive conductance signals of the membrane depletion/vortex phenomena, their
194 actuation and sensing time is also very rapid. With thin membranes and short nanoslots
195 (Fig. 2b), the ion depletion and hydrodynamic timescales range from microseconds to
196 seconds, allowing for rapid automation.
197   The ion current across an ion-selective medium can be very sensitive to the
198 charge polarity and density on the surface outside the medium. Our previous work
199 on alumina nanochannels demonstrates that with negatively charged SiO_2 entrance
200 side-walls, the ion conductance across the positive-charged Al_2O_3 nanochannel is
201 suppressed and shows a nonlinear *I–V* characteristic (Fig. 3a). The ion charge
202 inversion induced by the heterogeneous entrance charge enhances ion depletion

A Nanomembrane-Based Nucleic Acid Sensing Platform for Portable Diagnostics
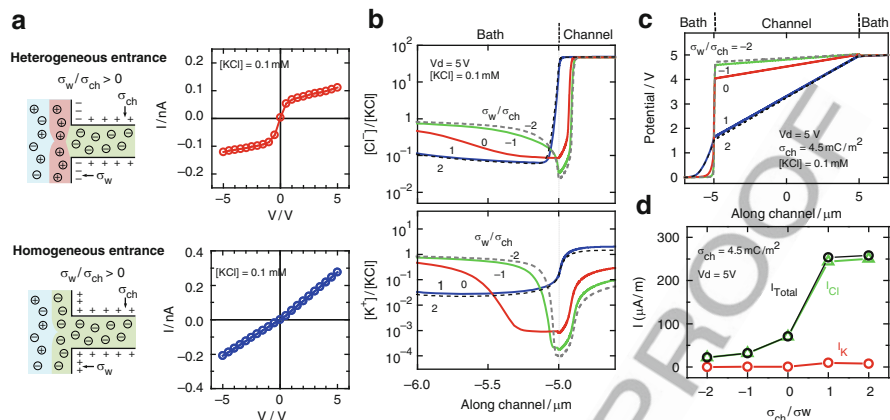
Fig. 3 Effect of entrance surface charge density and polarity on the ion transport in a 20-nm thick, 60-μm long, positively charged Al_2O_3 nanochannel. (**a**) Heterogeneous nanochannel entrance (the charge of entrance side-walls, σ_w and the charge of nanochannel σ_{ch} appear in opposite polarities, $\sigma_w/\sigma_{ch} < 0$) induces ion charge inversion at channel access. Experimental *I–V* characteristics of an Al_2O_3 nanochannel device with negatively charged silica entrance side-walls (*top*) and Al_2O_3 entrance side-walls (*bottom*) measured with 0.1 mM KCl. (**b**) Calculated Cl ion and K ion distributions near left channel entrance with values of σ_w/σ_{ch} varying from 2 to −2. (**c**) Calculated potential profile along the nanochannels with varied σ_w/σ_{ch} ($\sigma_{ch} = 4.5$ mC/m^2) under $V_d = 5$ V. (**d**) Summarized theoretical ion current density (current per channel width) of the nanochannels with varied σ_w/σ_{ch}

AU11

(Fig. 3b) and hence creates a large voltage drop at the channel entrance (Fig. 3c). The heterogeneous entrance charge efficiently suppresses the flow of counterions through the nanoslot (anions in the case of the positively charged Al_2O_3 nanochannel). This effect is clearly seen in Fig. 3d and is reflected in the measured *I–V* curves depicted in Fig. 3a. The ion conductance is found to change significantly when the surface charge of the entrance side-walls converts its polarity and density. The shift of ion conductance induced by surface charge conversion will be utilized as a basis of DNA/RNA sensing. Hybridization of DNA or RNA on a positively charged anion-selective medium can be detected by measuring the nonlinear *I–V* characteristics. 203 204 205 206 207 208 209 210 211

3   On-Chip Membrane Synthesis and Functionalization   212

Another key step is the proper development of surface chemistry to attach addressable probes onto different membrane sensors. This can be achieved by patterning UV-curable acrylic-based polymers inside the microfluidic channel doped with different monomers containing charged or functional groups. Such polymers are ion-selective and provide reactive chemical groups on their surfaces for the attachment of DNA/RNA probes. The functionality of all the devices proposed here relies on the ion-selectivity of the polymeric material, which is less dependent on 213 214 215 216 217 218 219

220 ionic strength than the nanofluidic counterparts. Briefly, using photolithographic
221 techniques, cation- and anion-exchange membranes are defined in glass microfluidic
222 channels by crosslinking positively charged diallyldimethylammonium (DADMA)
223 and negatively charged 2-acrylamido-2-methyl-1-propanesulfonic acid (AMPSA)
224 using a crosslinker (N, N'-methylene bisacrylamide) and photo-initiator. Each mem-
225 brane has a defined width and length of few tens to hundreds of micrometers, bridging
226 two microfluidic channels that are about 20 μm deep and 20–100 μm wide. The pore
227 size of the nanoporous membrane can be controlled by varying the concentration of
228 the monomers and crosslinker. To achieve surface functionalization of the oligo
229 probes, the surface of an anion-exchange membrane is modified with amino groups
230 by using allylamine as an additive in the prepolymer solution. The DNA or RNA
231 probe (~27 bases) pre-attached with functional groups of choice can then be used to
232 functionalize the probes onto membrane surface. Through examination by micro-
233 scope and measurement of the ability to deplete ions, the polymerization time and the
234 concentrations of crosslinker and photo-initiator have been optimized to produce
235 reproducible, well-defined ion-selective membranes with functional chemical groups
236 inside microchannels.

237   In Fig. 4, we show the first experimental evidence that the onset voltage and the
238 onset of overlimiting current, key features of the nonlinear $I–V$ curve of our sensor,
239 are sensitive to nucleic acid hybridization onto oligo probes functionalized onto the
240 surface of the ion-selective medium, as the resulting change in the surface charge
241 can enhance or eliminate the extended Debye layer. The voltage differential is
242 particularly large because of the nearly infinite differential resistance at the limiting
243 current conditions. In contrast, the low-voltage linear ohmic region, where classical
244 electrochemical sensors operate, registers an insignificant shift. Most conveniently,
245 the depleted and extended double layer, which can be three orders of magnitude
246 thicker than the Debye layer, also allows more charges on the target RNA to
247 contribute to the effective surface charge. If the membrane is oppositely charged
248 from the hybridized or functionalized molecules, the latter can even invert the
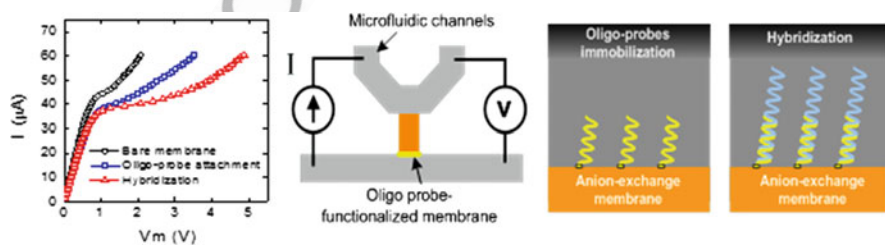249 charge on the membrane surface, eliminating the overlimiting current completely

Fig. 4 Ion-selective membrane as a sensitive sensor for the detection of biomolecules. *Left*:
Significant change of $I–V$ characteristics in the overlimiting current regime is observed after
RNA hybridization from a picomolar sample. The 50% change in conductance is compared to
typical 5% changes of electrochemical electrode sensors at the same concentration (low-voltage
region). *Center*: Diagram of sensor showing position of membrane. *Right*: Nucleic acid hybridiza-
tion onto immobilized oligoprobes

when the surface is effective electroneutral with exact compensation. The result is a very sensitive RNA sensor with picomolar sensitivity, compared to the nanomolar sensitivity of most electrode electrochemical sensors, as seen in Fig. 4.

4 Dielectrophoretic and Electrokinetic Molecular Concentration

Dielectrophoresis (DEP), a molecular force due to induced molecular dipoles, has been shown to be an effective means of concentrating large DNA/RNA molecules into the depleted region near the membrane surface (see Figs. 3, 4) where the probes are functionalized [9–12]. The electric field is focused by the nanopores in the membrane to produce a high field gradient at the membrane interface. A polarizable molecule in the bulk, with a large induced dipole, would then experience a net force towards the high-field region (the membrane surface). With the intense field amplification of nanopores, this DEP force on the molecules can overcome molecule–membrane repulsive interaction.

In a recent fluorescent correlation spectroscopy (FCS) experiment in collaboration with Yongjin Zhu (University of Pennsylvania), our laboratory was able to confirm this domination of dielectrophoretic attraction over like-charge repulsion with floating probe-functionalized carbon nanotubes (CNTs) and the fluorescently labeled kilobase target single-stranded DNA (ssDNA). Because CNTs quench the fluorophores on hybridization of target DNA, reduction in the fluorescent intensity can be used to quantify the hybridization degree and the attraction of the molecules to the nanoelectrode. As seen in Fig. 5, dielectrophoretic attraction due to the field-focusing
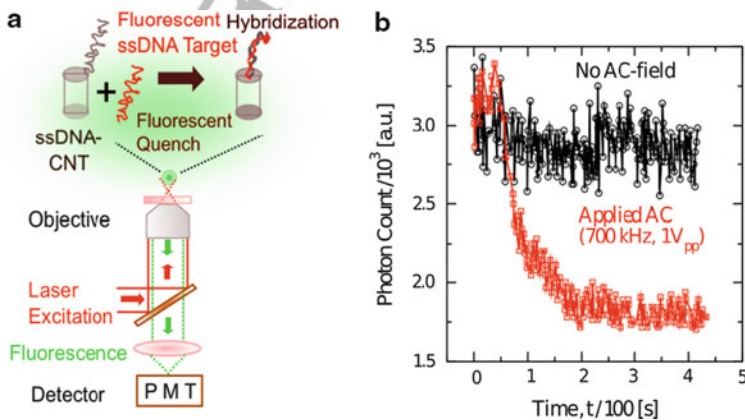
AU13

This figure will be printed in b/w

Fig. 5 (**a**) FCS detection of DNA hybridization from a picomolar solution. (**b**) Accelerated DNA fluorescence quench upon DNA docking with oligo-functionalized CNT probe under AC fields, in sharp contrast to the hour-long diffusive docking process without AC-fields

272 CNTs allows hybridization in less than 2 min at picomolar concentrations. In
273 contrast, the diffusion time for the long ssDNA at this concentration is hours.

274 Instead of floating nanoelectrodes (CNTs), our laboratory [3–7] is able to
275 fabricate 50-nm nanoslots on glass (inset in Fig. 3b) and is able to show concentra-
276 tion of ssDNA to the nanoslot. The same DNA concentration is shown with
277 nanoporous membranes in Fig. 3, with a concentration factor of up to five orders
278 of magnitude. Alternatively, 100-nm nanocolloids can be assembled into a nano-
279 colloid crystal (a membrane) at a top-down electrode pair by nanocolloid DEP
280 (Figs. 1c, 6). The 10 nm spacing between the nanocolloids focuses the electric field
281 of the electrode gate and can rapidly (order of seconds) trap and concentrate ssDNA
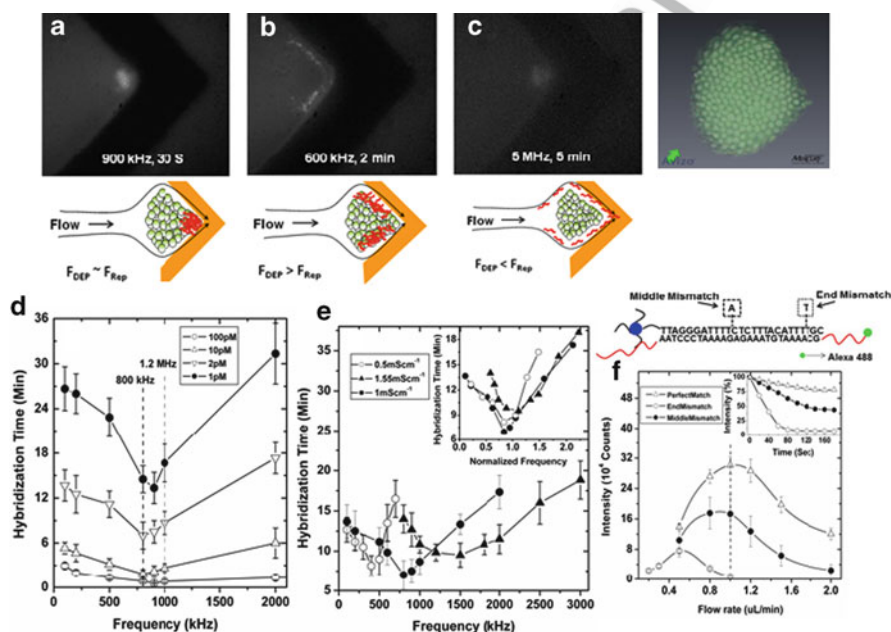
Fig. 6 (**a–c**) Fluorescence images of the trapping electrode tip in Fig. 2, showing the 100-nm
nanocolloid assembly (see SEM image on the *right*) at fixed times after the Green Crab DNA
solution had been injected but at different AC frequencies. The fluorescence is detectable only
when the ssDNA is concentrated beyond the micromolar level from the undetectable concentra-
tions (nanomolar to picomolar) of the injected solution. The DNA trapping location is further
clarified in the schematics below the images. Trapping at the assembly is achieved at low
frequencies, whereas none occurs at high frequencies. F_{DEP} dielectrophoretic force, F_{Rep} repulsive
force. (**d**) Detection time increases with decreasing concentration. (**e**) There is an optimum
frequency with a sharp minimum in detection time, which scales as $D/\lambda 2$ where λ is the Debye
length for the given electrolyte strength. (**f**) Fluorescence intensity at 2 min from different flow
rates of 100 pM of a 1 kb ssDNA target from a Green Crab species with a 26 base docking segment
in the middle and with a complementary 26 base oligo on the nanocolloid (*solid triangle*) or with a
single mismatch (*open triangle*). The flow rate window with single-mismatch discrimination is
indicated by a *vertical dashed line*. The scheme above the plot shows the actual 26 base ssDNA
docking sequence and the location of mismatched bases

AU14

AU15

AU16

molecules of a Green Crab species [3] from a picomolar solution onto the on-chip nanocolloid membrane by molecular DEP. A properly tuned DEP force can drive the DNAs towards the nanostructure against electrostatic repulsion from the like-charged structures, but they will not deposit onto the surface until they are convected to a sharp tip (~10 μm) at the nanostructure (Fig. 6a); intermolecular interaction can be adjusted to minimize nonspecific binding. A concentration factor exceeding 10^5 within minutes is observed from the fluorescent imaging in Fig. 6, thus rapidly and significantly enhancing the sensitivity of any sensor at the trapping location. The shear rate and AC frequency can be optimized so that the sensor can selectively discriminate against kilobase target molecules with a single mismatch in the 26 base pairing segment in the middle (Fig. 6f). This shear-enhanced selectivity eliminates the need for rinsing and washing steps.

Apart from dielectrophoretic concentration, which is not effective for small nucleic acids because the DEP force scales as the cubed power of the hydrodynamic radius of the molecule, our group has successfully demonstrated rapid analyte preconcentration based on ion depletion at an ion-selective membrane in microfluidic chips. As shown in Fig. 7a, a cation-exchange membrane UV-polymerized in a microslot bridging two microfluidic channels can induce deionization under voltage biases. The ion-depletion region functioning as an energy barrier traps the molecule passing across it in an electroosmotic flow tangential to the membrane on the side. The UV-curable ion-selective membrane offers superior concentration efficiency and proccessability compared to the microfabricated nanochannels reported previously [21, 22] or Nafion resins [23, 24]. Unlike the 100-nm thick nanochannels and surface-patterned Nafion thin films, the proposed membrane slot has the same depth as the microfluidic channel, yielding a large junction area. The large cross-section area provides greater ion current and better control of ion-depletion in the microchannels. Therefore, preconcentration can be achieved in few seconds. The fluorescence image in Fig. 7b shows the concentration of labeled molecules by several orders of magnitude in 10 s from a solution being pumped by
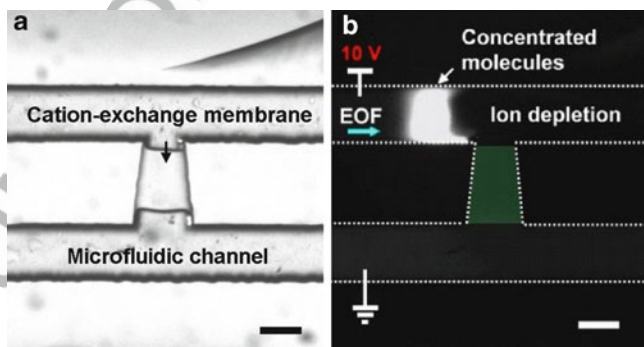

Fig. 7 (**a**) Optical microscopic image of a preconcentrator based on a charge-selective membrane. (**b**) Concentration of fluorescently labeled molecules taking place 10 s after applying a voltage bias of 10 V. Scale bars: 50 μm. *EOF* electroosmotic flow

This figure will be printed in b/w

311 electro-osmosis from the left to right in the top microfluidic channel, after 10 V is
312 applied across the membrane. Moreover, the proposed membrane adheres to acryl-
313 functionalized glass surfaces well; whereas Nafion has poor adhesion to most solid
314 surfaces and the process is more operator-dependent.

5 Polarization and Warburg Impedance Signals of Membrane Sensors: Label-Free and Non-Optical Detection

317 The presence of the docked RNA/DNA and their mobile counterions produce a
318 large conductivity change at the depleted region, which is where most of the voltage
319 drop occurs. Moreover, the extended Debye (polarization) layer [4, 25] allows more
320 of the charges on a long (>2 nm) DNA/RNA molecule to contribute to the charging
321 capacitance and surface-charge compensation on the surface. As described earlier,
322 the surface charge can sensitively alter the onset voltage for microvortices and the
323 overlimiting currents that the vortices contribute to. These effects greatly enhance
324 the capacitance, conductance and polarization signatures of the docked nucleic
325 acids, resulting in sensitive nonlinear I–V polarization signatures, such as those due
326 to the charge-inversion after hybridization in Fig. 4.

327 The dynamics of depletion layer formation with strong charging also exhibits
328 a distinct capacitance signature in the AC impedance spectrum (Fig. 8a). This
329 Warburg spectrum has a constant phase angle of $\pi/4$, whose modulus increases
330 with decreasing frequency and is classically associated with diffusion controlled
331 ion transport. In a recent paper [7], we have shown that, under an AC field,
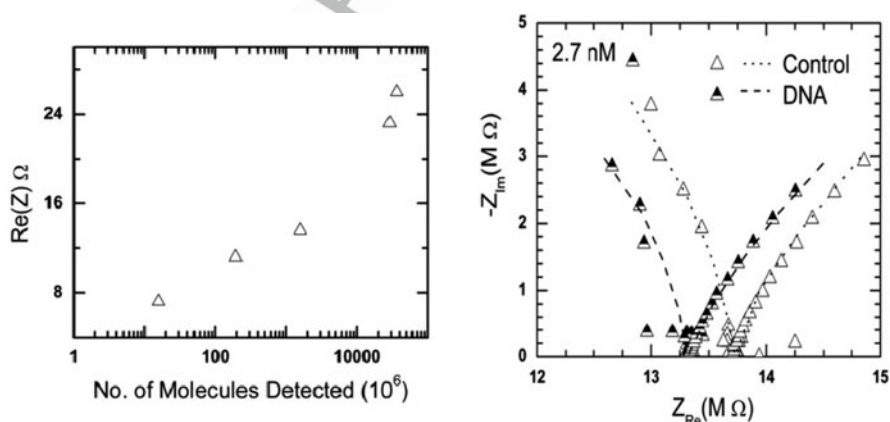332 the depletion region next to a membrane sensor is created periodically during the

Fig. 8 (**a**) Warburg impedance spectrum of the nanoslot in Fig. 2b, showing a shift to lower resistance with a 2.7 nM 1 kb *E. coli* ssDNA solution relative to the control without DNA. (**b**) The shift in the intercept with the real axis allows precise quantification of the number of ssDNA molecules in the microreservoir down to 10^7 copies

half-cycle when the mobile counterions are driven into the nanoslot or on-chip membrane. The depletion layer dynamics was verified by high-speed confocal imaging to be a diffusive one such that its thickness grows in a self-similar manner as $\sqrt{Dt}$ [5] and was shown to exhibit the Warburg spectrum, with a constant phase of $\pi/4$ (Fig. 8a). The intercept of the Warburg spectrum with the real axis represents the limiting ion flux when the depletion layer is smallest in dimension – just above the critical voltage where the depletion phenomenon can be sustained. It hence offers an accurate estimate of the low conductivity in this small region, as most of the voltage drop occurs there. As mentioned earlier, the presence of a few macro-ions attracted to this small depleted region by DEP can significantly change its local conductance. In Fig. 8b, we indicate sensitive detection of *E. coli* ssDNA below nanomolar concentrations or 10^7 molecules. With a reduction of the nanoslot width, down to the micrometer size of the nanocolloid assembly in Fig. 6, the detection limit is expected to reach below picomolar concentrations or 10^5 copies of nucleic acid. The same Warburg signal can be captured with the field across the nanocolloid assembly of Fig. 6 to allow label-free quantification of the docked DNA/RNAs. This large-voltage AC impedance technique is quite distinct from the classical low-amplitude impedance spectroscopy for electron transfer rates because we induce nonequilibrium ion transport through the ion-selective nanoslot or membrane to produce extended polarized Debye layer and concentration depletion layers.

6 Selectivity Enhancement

The single mismatch (SNP) discrimination capability of the experiment shown in Fig. 6f is due to hydrodynamic shear. In a recent MD project [15], it has been shown that shear is most discriminating because it can meter small thermal-energy-level
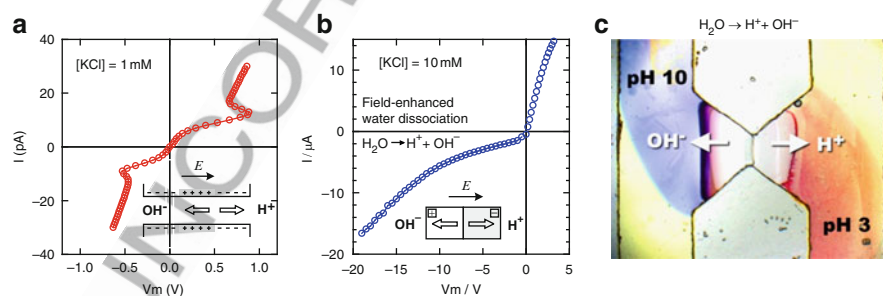
Fig. 9 Field-enhanced water dissociation increases ionic currents in (**a**) a reverse-biased 20-nm thick bipolar-junction nanofluidic channel containing positive and negative surface charges ($|V_m| > 0.6$ V), and (**b**) a UV-polymerized bipolar membrane ($V_m < -10$ V). (**c**) Hydroxide ions and protons are produced at the bipolar membrane junction and transport to opposite sides of the membrane. The pH change of the solution in the microchannels can be observed with a mixture of universal pH indicator. Left half of the bipolar membrane is positively charged whereas the right half is negatively charged

357 hydrogen bond energies to dehybridize the target molecules. One of the co-authors
358 (S.Z.) and other groups have recently developed microscale bipolar membrane
359 technologies that can be used to control the local pH in microfluidic chips to improve
360 both the specificity and selectivity of the membrane sensor [26, 27]. These bipolar
361 membranes/nanopores exhibit distinct hysteretic *I–V* polarization and cyclic voltam-
362 metry signatures due to local field-induced water-breaking reactions that generate
363 more ions [25, 26, 28–30]. An image of the pH fronts generated by a UV-polymerized
364 bipolar membrane composed of positively charged dimethylammonium and nega-
365 tively charged sulfonic groups are shown in Fig. 9. It was found that the ion currents
366 can drastically increase when reversely biased at a high voltage, forming a break-
367 down regime. In accordance with the second Wien effect, the ionic current break-
368 down results from the enhanced water dissociation into cation (H^+) and anion (OH^-)
369 at the bipolar junction, in which a strong electric field greater than 10 MV/cm can
370 build up at a reverse bias [29, 30]. These membrane actuation components can be
371 used to control the local pH for our integrated devices, with feedback control based
372 on the distinctive hysteretic polarization signals and *I–V* characteristics seen in Fig. 9.

373 7 Integrated Units

374 Other than the nanoslot chip of Fig. 2 and the DEP chip of Figs. 1, 6 for nanocolloid
375 assemblies, our group has integrated several components into the first-generation of
376 passive sensor chips [2–7]. One prototype is shown in Fig. 10. An assembly of
377 oligo-functionalized CNTs (a CNT membrane) is used to effect the ion depletion
378 and the Warburg quantification (Fig. 8) of hybridized ssDNA from a Green Crab
379 invasive species. The detection limit of the Warburg impedance signal is picomolar
380 concentrations or about the desired 10^5 copies, the detection time is about 15 min,
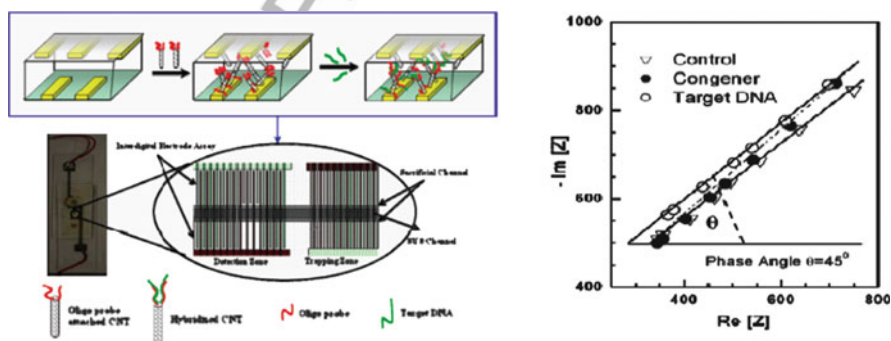

This figure will be printed in b/w

Fig. 10 *Left*: An integrated chip that uses an interdigitated electrode array to assemble oligo-functionalized CNTs into an ion-selective membrane. *Right*: The Warburg signal measured across the CNT assembly is able to detect picomolar concentrations (10^5 copies) of a kilobase-long DNA from a Green Crab species and differentiate a congener species with three mismatches over the 26 pair docking segment due to the hydrodynamic shear offered by the high through flow
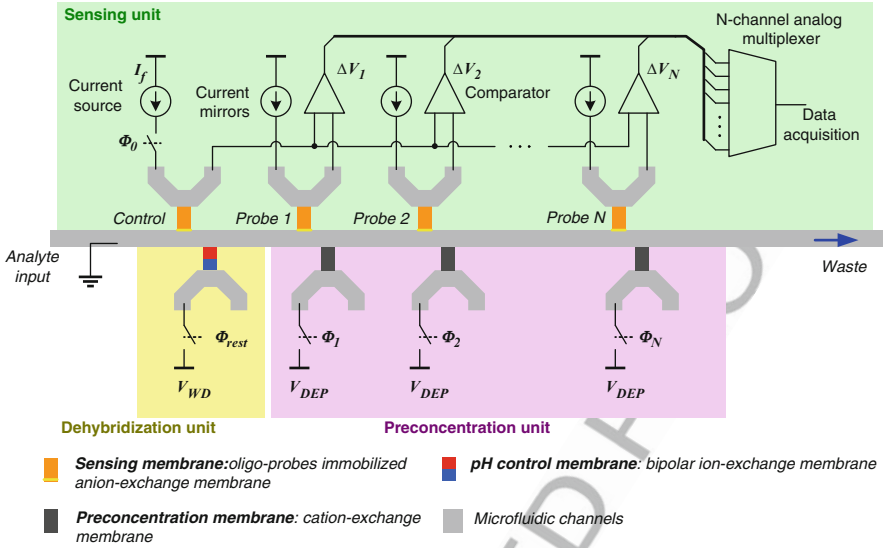
A Nanomembrane-Based Nucleic Acid Sensing Platform for Portable Diagnostics

Fig. 11 *Top*: Integrated smart RNA hybridization sensor composed of sensing unit, preconcentration unit, and dehybridization unit. *Bottom*: A functioning prototype measuring $10 \times 5 \times 15$ cm is shown in which a glass chip (like that shown in Fig. 10 but containing the multitarget design) is seen at the top of the instrumentation. A handheld prototype is expected in a year

and the selectivity is three mismatches in the 27 base pairing segments. The study showed that long kilobase target ssDNA produces a larger signal, consistent with the theory that the extended Debye layer allows more of the charges of a long molecule to contribute to the local charge capacitance and conductance.

A multitarget unit currently being developed is shown in Fig. 11. It offers sequential detection of different targets by moving the sample from one sensor

387 location to the next with the depletion technique. Such a design has been developed
388 for small sample volumes. For larger volumes, a parallel design can be implemen-
389 ted. These multitarget chips and the peripheral instrumentation are being developed
390 by FCubed LLC (http://www.FCubed.iviehost.com). A functioning prototype is
391 shown at the bottom of Fig. 11.

8 Conclusion and Commercialization Issues

393 Nanoporous membranes can greatly enable and sensitize on-chip molecular sensing.
394 They can deplete inhibitors near their surface where the probes are functionalized,
395 such that the platform is robust to a large variety of sample ionic strengths and pH.
396 More importantly, the same ion-depletion dynamics extends the Debye layer and
397 hence allows more sensitive conductance and capacitance detection of the hybridized
398 molecules. The high field in the same depletion region can produce fast dielectro-
399 phoretic trapping of the larger target molecules. If the depletion region extends across
400 the entire flow channel, it can also trap smaller molecules. Hence, by activating
401 different membrane components on a chip, the molecules can be concentrated and
402 transported to different sensors. The membrane's ability to invert its surface charge
403 upon hybridization produces a large conductance signal for hybridization. A large
404 capacitance signal is also produced, corresponding to the intercept of the Warburg
405 spectrum with the real axis, when the depletion layer is formed periodically under an
406 AC field such that the hybridized target molecules and their counterions are responsi-
407 ble for this asymptotic conductance when all other ions are depleted within the small
408 depletion layer. These nanoporous membranes are fabricated on the chip and are
409 situated on the side of the flowing channel without blocking the flow, such that a high
410 throughput (>1 μL/min) can be achieved. Bipolar nanoporous membranes can also be
411 used to split water and to exercise precise control of pH near the sensor, to enhance
412 selectivity. This rapid and precise pH control can also allow multitarget sensing with
413 the same probe if the probes are designed to be pH-sensitive.

414 Although the current membranes are synthesized on glass chips to allow easy
415 inspection and testing, the same technology can be transferred to hard polymer
416 chips, which should be cheaper to produce and easier to bond. This remains the final
417 obstacle to commercialization.

References

421   1. Deana A, Celesnik H, Belasco JG (2008) Nature 451:355
422   2. Basuray S, Senapati S, Ajian A, Mahon AR, Chang H-C (2009) ACS Nano 3:1823
423   3. Cheng I-F, Senapati S, Cheng X, Basuray S, Chang H-C (2010) Lab Chip 10:828

A Nanomembrane-Based Nucleic Acid Sensing Platform for Portable Diagnostics

4. Chang H-C, Yossifon G (2009) Biomicrofluidics 3:012001   424
5. Yossifon G, Chang H-C (2008) Phys Rev Lett 101:254501   425
6. Yossifon G, Chang Y-C, Chang H-C (2009) Phys Rev Lett 103:154502   426
7. Yossifon G, Mushenheim P, Chang Y-C, Chang H-C (2009) Phys Rev E 79:046305   427
8. Cady NC, Stelick S, Kunnavakkam M, Batt CA (2005) Sens Actuators B 107:332–341   428
9. Bakker E, Qin Y (2006) Anal Chem 78:3965   429
10. Umezawa Y, Aoki H (2004) Anal Chem 76:321   430
11. Basuray S, Chang H-C (2010) Biomicrofluidics 4:013205   431
12. Suni II (2008) Trends Anal Chem 27:604   432
13. Stern E, Wagner R, Sigworth FJ, Breaker R, Fahmy TM, Reed MA (2007) Nanolett 7:3405   433
14. Sosnowski R, Tu E, Butler WF, O'Conell JP, Heller MJ (1997) Proc Natl Acad Sci USA 94:1119   434 435
15. Kreft J, Chen YL, Chang H-C (2008) Phys Rev E 77:030801   436
16. Lin HT, Tsai LC, Chi PY, Chen CD (2005) Nanotechnology 16:2738   437
17. Wang P, Chen Z, Chang H-C (2006) Sens Actuators 113:500   438
18. Wang P, Chen Z, Chang H-C (2006) Electrophoresis 27:3964   439
19. Senapati S, Mahon SR, Gordon J, Nowak C, Sengupta S, Powell THW, Feder J, Lodge DM, Chang H-C (2009) Biomicrofluidics 3:022407   440 441
20. Ben Y, Chang H-C (2002) J Fluid Mech 461:229   442
21. Cheng L-J, Guo LJ (2010) Microfluid Nanofluid 9:1033   443
22. Wang Y-C, Stevens A, Han J (2005) Anal Chem 77:4293   444
23. Lee JH, Song Y-A, Han J (2008) Lab Chip 8:596   445
24. Liu V, Song YAK, Han J (2010) Lab Chip 10:1485   446
25. Cheng L-J, Guo LJ (2009) ACS Nano 3:575   447
26. Slouka Z, Pribyl M, Snita D, Postler T (2007) Phys Chem Chem Phys 9:5374   448
27. Zhang H, Mitrovski SM, Nuzzo RG (2007) Anal Chem 79:9014   449
28. Onsager L (1934) J Chem Phys 2:559   450
29. Ramirez P, Manzanares JA, Mafé S (1991) Ber Bunsenges Phys Chem 95:499   451
30. Mafé S, Manzanares JA, Ramirez P (1990) Phys Rev A 42:6245   452

Author Queries

Chapter No.: 142

Query Refs.	Details Required	Author's response
AU1	Please check if the edits made to the sentence "Most importantly, the assay…" is appropriate.	
AU2	Note that SAM is usually used for self-assembled monolayers. Please check.	
AU3	Please confirm that change to kb is correct.	
AU4	Please check added section number and other edits to this sentence is appropriate.	
AU5	Please confirm that added description of part (c) is correct.	
AU6	Please confirm that "deionized" is correct.	
AU7	Please check added figure parts for Fig. 2 is appropriate.	
AU8	The different parts of Fig. 2 need explanation. Please check the added suggestions carefully and make any necessary changes.	
AU9	The text states five orders. Please check.	
AU10	Note that the figure legend states six orders of magnitude. Please check.	
AU11	Please say what V_d signifies.	
AU12	Please check added suggested descriptions of images in Fig. 4. What does V_m signify?	
AU13	Please check added first name and affiliation for Zhu.	
AU14	Please confirm that image on the right is meant.	
AU15	Please check added explanation for F_{DEP} and $F_{Rep.}$	
AU16	Description of Fig. 2f does not seem to coincide with the figure. Please check.	
AU17	Please check S.Z.	